



# NASA Public Access

Author manuscript

*IEEE Trans Aerosp Electron Syst.* Author manuscript; available in PMC 2021 October 01.

Published in final edited form as:

*IEEE Trans Aerosp Electron Syst.* 2020 October ; 56(5): 3384–3393. doi:10.1109/taes.2020.2972248.

## Kalman Filter-based Robust Closed-loop Carrier Tracking of Airborne GNSS Radio-Occultation Signals

**Yang Wang [Student Member, IEEE],**

Ann & H.J. Smead Department of Aerospace Engineering Sciences, University of Colorado  
Boulder, Boulder, CO, USA

**Rong Yang,**

Shanghai Jiaotong University, China

**Yu T. Morton [Fellow, IEEE]**

Ann & H.J. Smead Department of Aerospace Engineering Sciences, University of Colorado  
Boulder, Boulder, CO, USA

### Abstract

GNSS radio occultation (RO) signals have been demonstrated as a viable means to retrieve atmospheric profiles. Current GNSS-RO observations rely on open-loop (OL) processing of the signals, especially for signals propagating through the lower troposphere. The reason is that GNSS signals at low elevations are adversely affected by multipath effects due to propagation through lower troposphere structures and reflections and scattering from the Earth surface. The low-elevation RO signals are characterized by deep and fast amplitude fading and rapid signal carrier phase fluctuations, collectively referred to as signal scintillation. The conventional phase-lock loop (PLL) may lose lock of these signals. While OL tracking is known for its robustness, its accuracy is determined by the climatological models used to create the reference for the GNSS signal carrier tracking loop. The wide bandwidth typically associated with OL tracking also introduces large errors in signal parameters estimations. In this paper, we present an adaptive Kalman filter-based closed-loop (KFC) tracking method, which takes into consideration the tropospheric scintillation, platform vibration, and real-time  $C/N_0$  estimation of the RO signals. The KFC method has comparable robustness with and improved accuracy over the OL tracking, which are demonstrated through comparison using real GPS RO data collected on an airborne platform. Analysis of the excess Doppler estimation, retrieved bending angles and impact parameters also confirms the improved performances of the proposed algorithm over OL tracking.

### Keywords

GNSS; Radio Occultation; Closed-loop; Kalman filter; Open-loop

## I. Introduction

Global Navigation Satellite System radio occultation (GNSS-RO) occurs when the satellite signal propagates through the atmosphere to reach a receiver from a low elevation angle. The gradient of the atmospheric refractive index leads to the bending of the signal ray path. By measuring the amount of the signal bending, profiles of atmospheric parameters such as temperature, humidity, and pressure can be derived. The concept of GNSS-RO was first demonstrated by the Global Positioning System Meteorology (GPS-MET) mission launched in April 1995 [1]–[3]. Since then, the GNSS-RO technique has been extensively studied and implemented on several low-earth orbit (LEO) satellite platforms, including COSMIC (Constellation Observing System for Meteorology, Ionosphere, and Climate) with a constellation of six remote sensing microsattellites [4], GRACE-FO (Gravity Recovery and Climate Experiment Follow-on) with a twin-satellite constellation as a successor to the GRACE mission [5], [6], the three MetOp satellites operated by European Organization for the Exploitation of Meteorological Satellites (EUMET-SAT) Polar System Programme [7] and the recently launched COSMIC-2 constellation. Thousands of daily profiles are now available from these missions, making GNSS-RO one of the top contributors to global weather modeling and forecasting [8]. Airborne and ground-based GNSS-RO are used to improve the regional availability of RO observations and to provide raw intermediate-frequency (IF) data to support study of RO signal structures to enable development of robust receiver algorithms [9]–[12].

The primary task of a GNSS-RO receiver is to estimate the excess Doppler of the RO signal, which is caused by the bending of the ray path. It is achieved through the carrier tracking loop of the receiver. The conventional GNSS closed-loop (CL) carrier tracking approach empirically chooses its filter parameters as a compromise between the dynamic requirements and the tracking sensitivity. However, low-elevation RO signals often experience strong scintillation characterized by fast and deep amplitude fading and large phase fluctuations caused by multipath propagation effects, which poses conflicting demands on the CL filter design. These multipath effects may originate from gradients in the atmospheric refractivity field and/or reflections and scattering from the Earth surface. Therefore, current GNSS-RO receivers are designed with open-loop (OL) tracking. The OL tracking algorithm relies on predicted excess Doppler frequency based on a climatological Doppler model and the relative motion between the receiver and the GNSS satellite, as described in [10], [13]. Though OL tracking is more robust than the conventional CL tracking, it has two important drawbacks. First, without a loop filter, OL tracking introduces a large amount of noise in the excess Doppler estimates. Second, in real applications, the accuracy of the climatological Doppler model is often at question, especially for the lower troposphere, and the error of the model will in turn bias the excess Doppler estimation and retrieved atmospheric parameters. Based on the GPS/MET data, [14] assessed the necessary bandwidth for an open-loop receiver, showing that the accuracy of the Doppler prediction model is about 15 Hz. For COSMIC, if the impact height is below 10 km, the mean difference between the Doppler observation and the Doppler model is about 8 Hz and the standard deviation of the differences is about 7 Hz [15]. According to [12], [16], an error of 5 Hz in the Doppler

model will lead to significant bias in the retrieved signal bending angles. Therefore, the retrieval of lower troposphere parameters is a serious challenge for OL-based RO receivers.

This paper presents a Kalman filter-based closed-loop (KFC) carrier tracking method for airborne GNSS RO receivers to track low-elevation signals. The KFC carrier tracking method is based on a generalized adaptive KF framework presented in [17], [18], which obtains its filter gain based on the process noise modelling and adaptive estimation of measurement noise covariance to improve robustness and accuracy. For RO receivers on an airborne platform, the vibration-induced oscillator noise and the signal propagation scintillation effects must be taken into consideration. In the proposed KFC algorithm described in this paper, the vibration and tropospheric phase scintillation effects are modeled as an equivalent degradation of oscillator phase noise power spectral density (PSD) and is implemented as modifications of the oscillator h-parameters. The amount of oscillator phase noise degradation is determined using real airborne RO measurements. The measurement noise covariance of the KFC implementation is based on the estimated high-rate  $C/N_0$ .

Real airborne GPS RO intermediate frequency (IF) data are used to test and evaluate the performance of KFC. The data collection experiment was conducted on September 13<sup>th</sup>, 2010 at ~13km altitude near Puerto Rico on the NSF/NCAR High-performance Instrumented Airborne Platform for Environmental Research (HIAPER) aircraft [19]. The performance of the KFC tracking is compared to OL tracking in terms of the robustness (capability in maintaining lock of signals) and the accuracy of excess Doppler estimation, the bending angles, and impact parameters retrieved via a Geometric Optics (GO) method as described in [20]. The results demonstrate that the KFC tracking can achieve comparable robustness with and better accuracy than the OL approach.

The organization of the rest of this paper is summarized as follows. Section II presents an analysis of the characteristics of a low-elevation GNSS-RO signal using real data. Section III describes the KFC tracking loop design. Section IV discusses the data collection experiment, data processing results, and comparative evaluations of the KFC tracking and the OL tracking performance. A conclusion and some planned future work are detailed in Section V.

## II. Low-elevation GNSS-RO Signal Characteristics

Low-elevation GNSS-RO signals experience bending when propagating through the lower troposphere. In addition, hydro-molecules and other atmospheric structures cause tropospheric scintillation, i.e., fast and deep amplitude fading and random carrier phase fluctuations. The tropospheric scintillation poses a challenge for conventional CL tracking methods to maintain lock of the signal. A good understanding of the disturbed RO signal characteristics is the foundation for developing techniques to mitigate the tropospheric scintillation effects. This section presents an analysis of real air-borne GNSS-RO data for this purpose.

Fig. 1 shows GPS PRN12  $C/N_0$  during a setting RO event, estimated at 1 Hz rate via the variance summation method (VSM) [21] and at 100 Hz rate based on signal intensity (SI) estimations using the method presented in [22]. The signal was processed using OL tracking.

Starting at around 2600s (since the start of data acquisition at 10:00 AM UTC on September 13<sup>th</sup>, 2010) when the satellite elevation angle is about  $2.5^\circ$  below horizon, deep fading with a magnitude up to 20 dB occurs. The mean  $C/N_0$  decreases as the elevation angle decreases. Conventional CL tracking methods lose lock shortly after 2600s. The zoomed-in section of  $C/N_0$  between 2800s and 2850s highlights the high rate signal amplitude fading. Clearly, the 1 Hz  $C/N_0$  estimations cannot capture the dynamic nature of the signal amplitude variations; thus, a high-rate  $C/N_0$  estimation is needed as the control parameter for adaptive implementation of a closed tracking loop, which will be discussed in detail in Section III.

Fig. 2 shows the detrended carrier phase and excess Doppler frequency from OL tracking outputs. The detrending is achieved by applying a 3-stage cascaded 6<sup>th</sup>-order Butterworth high-pass filter, with a cut-off frequency of 0.1 Hz [23]. Rapid, large carrier phase fluctuations with the magnitude reaching 2 carrier cycles can be observed, which impose challenges on CL tracking and impact its robustness and accuracy. The fluctuations in the excess Doppler estimates are also observed and are mainly due to tropospheric phase scintillation. OL tracking needs a prediction of the excess Doppler to generate reference signals. The excess Doppler is usually difficult to be accurately predicted as it is affected by weather and atmospheric conditions, especially at lower altitudes. For RO measurements performed on a LEO satellite, the excess Doppler could reach a few hundred Hz [14]. While OL tracking is robust to these tropospheric scintillation effects, its performance is dependent on the accuracy of the excess Doppler from a climatological model. More details about OL tracking's dependence on the climatological model will be discussed in Section IV.

### III. Algorithm Description

This section will present the KFC carrier tracking method for low-elevation RO signals. Current GNSS-RO receivers are implemented using OL tracking. For the sake of completeness, a brief summary of the OL tracking implementation based on [10], [19] is presented here. Fig. 3 shows the diagrams of OL tracking and KFC tracking architectures.

In OL tracking, the reference Doppler frequency is generated as the summation of the predicted excess Doppler, the line-of-sight (LOS) Doppler due to relative motion between the aircraft and GPS satellite, and the receiver clock drift. The prediction of excess Doppler follows the method described in [19]. It uses the Radio Occultation Simulator for Atmospheric Profiling (ROSAP) ray tracing program and the regional monthly mean refractivity profiles. The LOS Doppler frequency is obtained based on the GPS satellite position derived from the ephemeris and the aircraft position computed using high-elevation satellite signals in the recorded data. Due to errors in the Doppler model, there will be phase differences between the reference signal and the input RO signal. OL tracking uses a carrier phase discriminator, such as a two-quadrant arctan discriminator for a carrier with data modulation, to measure the carrier phase differences and to correct the accumulated Doppler range (ADR) of the reference signal. The raw OL estimates of excess Doppler are obtained by differentiating the corrected ADR. A filter or smoother is usually applied to the raw excess Doppler estimates before they are further processed to retrieve atmospheric profiles. In this paper, the filtering of excess Doppler consists of two steps for both KFC and OL tracking implementations. The first step uses a Hampel filter with a moving window of 10s

to remove outliers. The second step uses a median filter with a moving window of 5s to reduce noise.

The KFC method is developed based on the generalized KF framework as presented in [17], [18]. The KFC architecture is an expansion on this generalized CL tracking with two additional elements designed specifically to process low-elevation RO signals. The first element is the KF gain calculation, which takes into consideration the combined effects from platform dynamics, vibration-induced oscillator noise, and tropospheric phase scintillation. This is different from conventional CL tracking which uses a fixed filter noise bandwidth. It is also different from the typical KF-based CL tracking which only takes into consideration the oscillator noise and platform dynamics in the process noise. The second element is that the KF gain is controlled by real-time estimation of the SI. SI is a high rate estimation of signal power which captures the rapidly varying signal power fading level in a prompt manner. This is different from conventional adaptive filters which adjust their noise bandwidth or other control parameters according to the low-rate  $C/N_0$  estimation. In the following subsections, we will discuss each of the components in the KFC design below.

### A. State-Space System Models

We define the discrete-time carrier state vector  $\mathbf{x}_k = [\varphi \ \omega \ \dot{\omega}]_k^T$ , where its elements are carrier phase (rad), carrier frequency (rad/s), and carrier frequency rate (rad/s<sup>2</sup>) at epoch  $k$ . The following notations are used in the paper:

$\mathbf{x}_k$ : true state

$\hat{\mathbf{x}}_k$ : estimated state

$\tilde{\mathbf{x}}_k$ : predicted state, (for local replicas generation)

$\delta\mathbf{x}_k$ : error state, defined as  $\delta\mathbf{x}_k = \mathbf{x}_k - \tilde{\mathbf{x}}_k$

$\delta\hat{\mathbf{x}}_k$ : estimated error state

The signal dynamic model is represented as:

$$\mathbf{x}_{k+1} = \mathbf{A}\mathbf{x}_k + \mathbf{w}_k \quad (1)$$

where  $\mathbf{A}$  is the state transition matrix

$$\mathbf{A} = \begin{bmatrix} 1 & T & \frac{T^2}{2} \\ 0 & 1 & T \\ 0 & 0 & 1 \end{bmatrix} \quad (2)$$

and  $T$  is the integration time. We used  $T=10$  ms in this study for all OL and CL signal tracking.  $\mathbf{w}_k$  is the system dynamics noise vector with covariance matrix  $\mathbf{Q}$ .

The local carrier replicas are generated based on the predicted state  $\tilde{\mathbf{x}}_{k+1}$ , which is represented as

$$\tilde{\mathbf{x}}_{k+1} = \mathbf{A}(\tilde{\mathbf{x}}_k + \delta\hat{\mathbf{x}}_k) \quad (3)$$

From Equations (1) and (3), the error state dynamics equation can be obtained as:

$$\delta\mathbf{x}_{k+1} = \mathbf{A}(\delta\mathbf{x}_k - \delta\hat{\mathbf{x}}_k) + \mathbf{w}_k \quad (4)$$

The measurement model is represented as:

$$\delta\varphi_k = \mathbf{C}\delta\mathbf{x}_k + \mathbf{v}_k \quad (5)$$

where  $\delta\varphi_k$  is the carrier phase error,  $\mathbf{C}$  is the measurement transition matrix,

$$\mathbf{C} = \begin{bmatrix} 1 & T & T^2 \\ & 2 & 6 \end{bmatrix} \quad (6)$$

and  $\mathbf{v}_k$  is the measurement noise vector with covariance matrix  $\mathbf{R}$ .

The measurement of  $\delta\varphi_k$  is typically obtained by applying a phase discriminator. For a data-less pilot channel, a four-quadrant arctan function can be used, while for a channel with navigation data modulation, a two-quadrant arctan function can be used. Removing data bits and using four-quadrant phase discrimination can significantly improve OL results [24]. In this study, we will use the four-quadrant arctan function:

$$\delta\varphi_k = \arctan2(Q_k, I_k) \quad (7)$$

where  $I_k$  and  $Q_k$  are the in-phase and quadrature correlator outputs. The navigation data bits are removed using the COSMIC post-processed archive files.

Thus, combining Equations (4) and (5), the CL tracking process is abstracted into a Kalman filter-based carrier phase estimation problem:

$$\delta\hat{\mathbf{x}}_k = \mathbf{K}_k\delta\varphi_k \quad (8)$$

And the state vector is estimated as:

$$\hat{\mathbf{x}}_k = \tilde{\mathbf{x}}_k + \mathbf{K}_k\delta\varphi_k \quad (9)$$

where  $\mathbf{K}_k$  is the Kalman gain at epoch  $k$ .

## B. Process Noise Modelling

For airborne GPS RO signals, the process noise includes contributions from the platform dynamics, oscillator thermal noise, vibration-induced oscillator noise, and troposphere scintillation. The platform dynamics noise can be modelled by the receiver-satellite LOS acceleration variation in a unit interval, following the treatment presented in [25]. The

oscillator thermal noise is modelled by the oscillator h-parameters [26]. However, there is no existing model for the troposphere phase scintillation effects for low-elevation RO signals. Furthermore, the vibration effects are difficult to be distinguished from other noise effects. The approach we take in this study is to derive the combined troposphere scintillation and aircraft vibration effects based on the PSD of experimentally-obtained phase data. This combined effect is then used to modify the stationary receiver oscillator h-parameters. This approach is explained in detail below.

If the troposphere scintillation and aircraft vibration effects are not taken into consideration, the covariance of the process noise vector is modelled as:

$$\mathbf{Q} = (2\pi f_L)^2 \begin{bmatrix} Tq_\varphi + \frac{T^3}{3}q_\omega + \frac{T^5}{20}\frac{q_a}{c^2} & \frac{T^2}{2}q_\omega + \frac{T^4}{8}\frac{q_a}{c^2} & \frac{T^3}{6}\frac{q_a}{c^2} \\ \frac{T^2}{2}q_\omega + \frac{T^4}{8}\frac{q_a}{c^2} & Tq_\omega + \frac{T^3}{3}\frac{q_a}{c^2} & \frac{T^2}{2}\frac{q_a}{c^2} \\ \frac{T^3}{6}\frac{q_a}{c^2} & \frac{T^2}{2}\frac{q_a}{c^2} & T\frac{q_a}{c^2} \end{bmatrix} \quad (10)$$

where  $f_L$  is the carrier frequency,  $q_\varphi = \frac{h_0}{2}$  and  $q_\omega = 2\pi^2 h_{-2}$  are the receiver oscillator phase and frequency power spectral densities, respectively, and  $q_a$  is the PSD of the receiver-satellite LOS acceleration disturbances.  $h_0$  and  $h_{-2}$  are the oscillator h-parameters. The data used in this study was recorded using a reference signal from a Symmetricom ExacTime 6000 GPS receiver with an oven-controlled crystal oscillator (OCXO) [27]. Based on the specification sheet provided by the manufacturer, the stationary h-parameters are  $h_0 = 2.0 \times 10^{-23}$  (s<sup>2</sup>/Hz) and  $h_{-2} = 2.13 \times 10^{-24}$  (1/Hz).

To take into consideration of the troposphere scintillation and aircraft vibration, we examine the detrended phase noise PSDs of real airborne phase measurements. The detrending process removes low frequency components such as the satellite-receiver range, background ionosphere and troposphere refraction effects, etc. It is accomplished by filtering the raw phase measurements using a 6<sup>th</sup> order Butterworth high-pass filter with 0.1 Hz cutoff frequency [23]. Fig. 4 plots the PSDs of detrended carrier phase from 4 GPS RO events at various elevation angles using real data from the airborne experiment on September 13<sup>th</sup>, 2010. For each RO event, the PSD is computed for 6 segments of data: one segment for signal at 2° ~ 3° elevation angle and 5 segments for -5° ~ 0° (1° per segment). The purpose is to examine the carrier phase noise PSDs and their dependence on elevation angles. The oscillation phase noise and the aircraft vibration-induced additional oscillator phase jitter should be similar for these data segments in each RO event.

Visual examination of Fig. 4 indicates that the PSDs for RO signals at elevation angle below about -3° are drastically different from above -3°. The PSDs of carrier phase noise do not show significant dependence on the elevation angle for RO signals at below -3°. This observation is consistent for all 4 RO events. For RO signals with elevation above -3°, the carrier phase noise PSDs are mostly similar, although PRN12 has a slightly higher amplitude

which is most likely caused by contributions of weak tropospheric phase scintillation. Based on the altitude of the aircraft in this experiment, the  $-3^\circ$  elevation corresponds roughly to 8km tangent point altitude. The PSDs shown in Fig. 4 indicates that tropospheric scintillation effects become significant below 8km altitude at this location. While we expect that weather conditions will have an impact on the actual value of this altitude,  $-3^\circ$  will be treated as the nominal elevation, and real time PSD obtained for signals received below this nominal elevation will be used to model tropospheric scintillation.

Fig. 4 also shows the oscillator phase noise (including the vibration effects), which is extracted from the high-elevation spectrum where the scintillation effects is of less importance. We model the combined vibration effects and troposphere scintillation effects as an effective increase in the stationary oscillation phase noise. Fig. 5 plots 2 segments of the carrier phase PSDs for PRN 12 RO signal:  $[-5^\circ, -4^\circ]$  and  $[2^\circ, 3^\circ]$  elevation. The maximum separation of the two PSDs is  $\sim 23\text{dB}$  which occurs at around 1Hz. We may consider this separation to be due to the combined tropospheric scintillation and vibration-induced oscillator phase noise.

To quantitatively model the combined tropospheric scintillation and the vibration-induced oscillator phase noise, we computed the phase PSD for the OCXO used in the data collection experiment. The result is shown as the solid linear line in Fig. 5. We artificially degrade the oscillator PSD by adding the 23dB equivalent amount of the combined troposphere and vibration effects for the segment of the lower elevation signal  $[-5^\circ, -4^\circ]$ . The degraded PSD is plotted as the dashed linear line in Fig. 5. Based on the degraded oscillator PSD, we compute its equivalent h-parameters to be  $h_0 = 3.99 \times 10^{-21}$  ( $\text{s}^2/\text{Hz}$ ) and  $h_{-2} = 4.25 \times 10^{-22}$  ( $1/\text{Hz}$ ). This set of degraded h-parameters are used to compute the process noise covariance matrix in Equation (10) when tropospheric phase scintillation is detected.

### C. Adaptive Tuning of Kalman Filter

The performance of a KF depends on the estimation of the covariances for process noise and measurement noise at steady-state. At the transient stage of the process, the initial state error covariance matrix also impacts its performance. At steady-state, the Kalman gain can be calculated as:

$$\bar{\mathbf{K}} = \bar{\mathbf{P}}\mathbf{C}^T(\mathbf{R} + \mathbf{C}\bar{\mathbf{P}}\mathbf{C}^T)^{-1} \quad (11)$$

where  $\bar{\mathbf{P}}$  is the steady-state error covariance matrix. It can be solved from the Riccati equation [28]:

$$\bar{\mathbf{P}} = \mathbf{A}\bar{\mathbf{P}}\mathbf{A}^T - (\mathbf{A}\bar{\mathbf{P}}\mathbf{C}^T)(\mathbf{R} + \mathbf{C}\bar{\mathbf{P}}\mathbf{C}^T)^{-1}(\mathbf{C}\bar{\mathbf{P}}\mathbf{A}^T) + \mathbf{Q} \quad (12)$$

For low-elevation airborne RO signals with tropospheric scintillation, the  $\mathbf{Q}$  matrix can be computed based on the degraded oscillator h-parameters (see Equation 10). The measurement noise covariance is  $\mathbf{R} = \sigma_\varphi^2$ , where  $\sigma_\varphi^2$  can be computed based on the signal  $C/N_0$  and the integration time [29]:

We computed the steady-state Kalman gain matrix element for the low elevation segment ( $[-5^\circ, -4^\circ]$ ) signal, allowing  $C/N_0$  to vary from 15 dB-Hz to 60 dB-Hz and plotted the results in Fig. 6. To reduce computation, we fit polynomial curves to each element in the Kalman gain matrix. When a  $C/N_0$  is estimated, the steady-state Kalman gain can be directly calculated using the fitted polynomial parameters.

#### D. High-rate $C/N_0$ Estimation

To obtain the Kalman gain adaptively to capture the dynamic nature of signal amplitude variations caused by tropospheric scintillation, a high-rate  $C/N_0$  estimation is needed. The high-rate  $C/N_0$  is calculated based on the SI, as described in [22]. The process is briefly outlined here for the sake of completeness:

1. Compute  $C/N_0$  over a typical time span (such as 10 second) using the VSM method [21].
2. Compute  $SI$  by averaging the SI measurements during the same time span used to compute  $C/N_0$ .
3. Compute  $SI_H$ , the high rate SI for a short time interval within the long time span.
4. Compute  $C/N_{0H}$ , the high-rate  $C/N_0$  using:

$$C/N_{0H} = C/N_0 + (SI_H - SI) \quad (13)$$

### IV. Evaluation Using Experimental Data

Real airborne GPS L1 RO IF data was collected above the ocean near Puerto Rico on the HIAPER aircraft at about 13 km altitude on September 13<sup>th</sup>, 2010, 10:00 – 12:10 UTC and provided by UCSD [10]. In this study, GPS L1 CA signals for a setting (PRN 25) and a rising (PRN 20) RO events are used to demonstrate the performance of the proposed KFC algorithm. The flight path and the tangent point locations for the two events are shown in Fig. 7. The tangent point is the closest location along a RO ray path to the Earth's surface and where the ray path's bending occurs.

The GPS signal was received from a wide-view avionics antenna and sampled at 10 MHz and 1 bit resolution. The complex I/Q data was recorded to a disk array using the GNSS Recording System (GRS) developed by the Johns Hopkins University Applied Physics Laboratory [30]. A Symmetricom ExacTime 6000 GPS receiver with an OCXO was used to provide a 10 MHz reference signal to the GRS.

#### A. KFC and OL Tracking Performance Comparison

We compare the performance of KFC and OL tracking using data collected for the two RO events discussed above. Fig. 8(a) and Fig. 8(b) show the high-rate  $C/N_0$  (1Hz) and excess Doppler estimations for the PRN 25 (a setting RO event) and PNR 20 (a rising event), respectively. Also shown are the satellite elevation and climatological model for the excess Doppler used in the OL tracking. For the rising RO event, the tracking processes are applied

to the time reversed data sequence. For the OL tracking of PRN 25 RO signal, a climatological model is obtained from the CIRA-Q model and the ROSAP ray tracing program [19], while for the PRN 20 RO event, the Doppler model is obtained from polynomial fitting of the post-processing results.

The excess Doppler estimates are obtained by estimating the Doppler frequency of the received RO signal and subtracting the LOS Doppler frequency and the receiver clock drift. For KFC tracking, the Doppler frequency is directly obtained from the estimated state vector. For OL tracking, it is obtained by differentiating the estimated ADR and, in this paper, with a differentiation time interval of 100ms.

The  $C/N_0$  estimates from KFC and OL outputs show consistent trend and fluctuations for both RO events. Visual examination of the estimated  $C/N_0$  indicates that for both KFC and OL tracking there is a cut-off elevation under which the RO signals are too weak to allow meaningful estimations of signal parameters. The cut-off elevations are  $-5.3^\circ$  and  $-4.6^\circ$  for the PRN 25 and 20, respectively.

Above the cut-off elevation, the excess Doppler estimates by KFC, OL, and climatological model exhibit the consistent trend. The KFC excess Doppler estimates show smaller variations than the OL estimates. As expected, the OL excess Doppler estimates has larger noise than the KFC results.

## B. OL Dependence on Climatological Model

The excess Doppler from the climatological models used in this study are very close to the estimated excess Doppler using KFC and OL. In real applications, the accuracy of the climatological model cannot be guaranteed. This is especially the case for lower troposphere observations. An inaccurate climatological model will degrade the performance of the OL tracking and the subsequent retrieval of atmospheric parameters. For GNSS-RO on a LEO satellite, the uncertainty of the climatological model can be up to 15 Hz [15]. For KFC, a distinctive advantage is that it does not require Doppler model inputs, while its performance is dependent on the process noise and measurement noise modelling. To provide a quantitative assessment of the climatological model error impact on OL tracking, we artificially introduced  $\pm 5$  Hz bias to the climatological model. The biased models are applied to the OL tracking of the PRN 25 signal. The original and biased Doppler models, as well as the resulting excess Doppler estimates are plotted in Fig. 9. The comparison shows that OL tracking results are dependent on climatological models. A 5 Hz error in climatological model will cause up to 3 Hz bias in OL excess Doppler estimations when the  $C/N_0$  is low. The KFC tracking result is consistent with OL tracking using an unbiased climatological model.

## C. KFC Sensitivity on Process Noise Model

The KFC tracking performance is dependent on the tuning parameters, i.e. the process noise matrix  $\mathbf{Q}$  and measurement noise  $\mathbf{R}$ .

The  $C/N_0$ -based measurement noise model is well established in [29] and is a standard strategy for tuning the KF-based tracking loops. To assess the sensitivity of KFC

performance on the process noise model, we apply the process noise covariance  $\mathbf{Q}$  in Equation (10),  $1010\mathbf{Q}$ , and  $\mathbf{Q}/10$  to the KFC tracking. The estimated excess Doppler using these three process noise matrices are shown in Fig.10. It can be observed that the modelled process noise covariance in Section III (B) leads to the best performance of KFC tracking, increasing  $\mathbf{Q}$  causes noisier estimates while decreasing  $\mathbf{Q}$  causes earlier loss of lock of the signal. The KFC tracking with all these three covariance matrices provide somewhat satisfactory results, so the KFC results are not too sensitive to the process noise modelling.

#### D. Bending Angle and Impact Height

To further evaluate the performance of KFC tracking and the impact of biased OL excess Doppler estimates due to inaccurate climatological models, the bending angles against impact heights are retrieved via a Geometric Optics approach as described in [19], [20]. Fig. 11 shows the retrieved bending angles and impact heights from PRN 25 RO event using the estimated excess Doppler by KFC and OL with the original and biased climatological models and the retrieved refractivity as compared with the dropsonde observation.

It can be observed from Fig.11(a) that RO measurements can be retrieved from the aircraft's height to an altitude of about 2 km. The bending angle retrievals from KFC tracking results are very close to those from OL tracking with a good climatological model. The biased climatological models cause large bias to the retrieved bending angles which can be up to about  $0.6^\circ$ . This analysis clearly demonstrated that the KFC tracking not only provides comparable robustness to that of the OL, it also offers accuracy comparable to OL with an accurate climate model. While the OL tracking performance is dependent on the climatological model, which is usually not accurate for the lower troposphere, the KFC does not require such a model input.

It should be noted that the Geometric Optics retrieval method is not adequate for retrieving bending angles in the lower troposphere [20]. A dropsonde experiment was conducted at  $[16.8624\text{N}^\circ, 76.9897\text{W}^\circ]$  (as shown in Fig.7) and at 18:47 UTC, September 13, 2010. As shown in Fig. 11(b), the retrieved refractivity from the PRN 25 RO event consists with the observation from a dropsonde experiment above 6 km, while has significant error below 6 km. To better assess the RO retrievals of the troposphere, the wave optics approaches [19], [31] should be applied.

#### V. Conclusion and Discussion

This paper presents a robust and accurate KF-based closed-loop tracking method for airborne GNSS RO signals traversing the lower troposphere. The KFC method models the combined troposphere scintillation and vibration-induced oscillator effects for GNSS RO receivers onboard an aircraft as degraded stationary oscillator noise. Real airborne RO experimental data are used to quantitatively derive the amount of degradation for low-elevation satellite signals and to translate the degradation in terms of oscillator h-parameters modifications.

The method performance is demonstrated by processing real airborne GPS RO data and comparing it to an OL implementation. The results indicate that both KFC and OL can

retrieve bending angles to an impact height of about 2km in this particular set of data. The results also show that KFC and OL can achieve similar robustness and accuracy, if an accurate climatological Doppler model is available to the OL. The impact of the Doppler model accuracy on OL tracking is further investigated by artificially introduced biases. A 5 Hz Doppler model bias yields about 2 Hz OL tracking error and about  $0.6^\circ$  bending angle error during low  $C/N_0$  segments. These errors are significant. The Geometric Optics approach is used in this paper to retrieve bending angles and impact parameters which is problematic for the lower troposphere (altitude  $< 6$  km). The wave optics approaches will be applied in the future work.

The experimental data used in this paper is limited by the antenna gain which only allows signal tracking to 2 km tangent point height. This limitation made it difficult to observe and model the effects of troposphere scintillation, Earth surface scattering, and oscillator vibration. In a subsequent study, airborne and mountain-top based RO experiments with a high-gain antenna have been conducted, and their results have been used to evaluate the RO observations of the lower troposphere [11] and to enable separation of tropospheric scintillation from surface reflections [32]. These studies will allow further improvement of the troposphere phase scintillation noise models.

## Acknowledgment

The authors would like to thank Dr. Jennifer S. Haase from Scripps Institution of Oceanography for providing the airborne data and assisting in generating the climatological models. The project is supported by NASA grant #NNX15AT54G and University of Colorado Boulder.

This work was supported by NASA grant # NNX15AT54G and University of Colorado Boulder.

## References

- [1]. Kursinski E, Hajj G, Bertiger W, Leroy S, Meehan T, Romans L, Schofield J, McCleese D, Melbourne W, Thornton C et al., "Initial results of radio occultation observations of Earth's atmosphere using the Global Positioning System," *Science*, vol. 271, no. 5252, pp. 1107–1110, 1996.
- [2]. Kursinski E, Hajj G, Schofield J, Linfield R, and Hardy KR, "Observing Earth's atmosphere with radio occultation measurements using the Global Positioning System," *Journal of Geophysical Research: Atmospheres*, vol. 102, no. D19, pp. 23429–23465, 1997.
- [3]. Ware R, Exner M, Feng D, Gorbunov M, Hardy K, Herman B, Kuo Y, Meehan T, Melbourne W, Rocken C et al., "GPS sounding of the atmosphere from low Earth orbit: Preliminary results," *Bulletin of the American Meteorological Society*, vol. 77, no. 1, pp. 19–40, 1996.
- [4]. Cook K, Fong C-J, Wenkel MJ, Wilczynski P, Yen N, and Chang G, "FORMOSAT-7/COSMIC-2 GNSS radio occultation constellation mission for global weather monitoring," in *2013 IEEE Aerospace Conference IEEE*, 2013, pp. 1–8.
- [5]. Beyerle G, Schmidt T, Michalak G, Heise S, Wickert J, and Reigber C, "GPS radio occultation with GRACE: Atmospheric profiling utilizing the zero difference technique," *Geophysical Research Letters*, vol. 32, no. 13, 2005.
- [6]. Wickert J, Michalak G, Schmidt T, Beyerle G, Cheng C-Z, Healy SB, Heise S, Huang C-Y, Jakowski N, Kohler W et al., "GPS radio occultation: results from CHAMP, GRACE and FORMOSAT-3/COSMIC." *Terrestrial, Atmospheric & Oceanic Sciences*, vol. 20, no. 1, 2009.
- [7]. Von Engel A, Andres Y, Marquardt C, and Sancho F, "GRAS radio occultation on-board of Metop," *Advances in Space Research*, vol. 47, no. 2, pp. 336–347, 2011.

- [8]. Harnisch F, Healy S, Bauer P, and English S, "Scaling of GNSS radio occultation impact with observation number using an ensemble of data assimilations," *Monthly Weather Review*, vol. 141, no. 12, pp. 4395–4413, 2013.
- [9]. Haase J, Murphy B, Muradyan P, Nievinski F, Larson K, Garrison J, and Wang K-N, "First results from an airborne GPS radio occultation system for atmospheric profiling," *Geophysical Research Letters*, vol. 41, no. 5, pp. 1759–1765, 2014.
- [10]. Wang K-N, Garrison JL, Acikoz U, Haase JS, Murphy BJ, Muradyan P, and Lulich T, "Open-loop tracking of rising and setting GPS radio-occultation signals from an airborne platform: Signal model and error analysis," *IEEE Transactions on Geoscience and Remote Sensing*, vol. 54, no. 7, pp. 3967–3984, 2016.
- [11]. Morton Y, Bourne H, Taylor S, Xu D, Yang R, Graas F, and Pujara N, "Mountain-top radio occultation with multi-GNSS signals: experiment and preliminary results," in *Proceedings of the ION 2017 Pacific PNT Meeting*, 2017, pp. 490–499.
- [12]. Beyerle G and Zus F, "Open-loop GPS signal tracking at low elevation angles from a ground-based observation site," *Atmospheric Measurement Techniques*, vol. 10, no. 1, p. 15, 2017.
- [13]. Sokolovskiy S, Rocken C, Hunt D, Schreiner W, Johnson J, Masters D, and Esterhuizen S, "GPS profiling of the lower troposphere from space: Inversion and demodulation of the open-loop radio occultation signals," *Geophysical Research Letters*, vol. 33, no. 14, 2006.
- [14]. Sokolovskiy SV, "Tracking tropospheric radio occultation signals from low Earth orbit," *Radio Science*, vol. 36, no. 3, pp. 483–498, 2001.
- [15]. Xu YLYL, Xian-Sheng and Xu X, "Accuracy assessment of the Doppler frequency and pseudorange model based on GPS/LEO radio occultation," in *China Satellite Navigation Conference (CSNC) 2015 Proceedings: Volume I Springer Berlin Heidelberg*, 2015, pp. 3–12.
- [16]. Schreiner W, Sokolovskiy S, Hunt D, Rocken C, and Kuo Y-H, "Analysis of GPS radio occultation data from the FORMOSAT-3/COSMIC and Metop/GRAS missions at CDAAC," *Atmospheric Measurement Techniques*, vol. 4, no. 10, pp. 2255–2272, 2011.
- [17]. Yang R, Ling K-V, Poh E-K, and Morton Y, "Generalized GNSS signal carrier tracking: Part I-modeling and analysis," *IEEE Transactions on Aerospace and Electronic Systems*, vol. 53, no. 4, pp. 1781–1797, 2017.
- [18]. Yang R, Morton Y, Ling K-V, and Poh E-K, "Generalized GNSS signal carrier tracking: Part II-optimization and implementation," *IEEE Transactions on Aerospace and Electronic Systems*, vol. 53, no. 4, pp. 1798–1811, 2017.
- [19]. Wang K-N, "Signal analysis and radioholographic methods for airborne radio occultations," Ph.D. dissertation, School Aeron. Astronaut., Purdue University, West Lafayette, IN, USA, Dec. 2015.
- [20]. Murphy B, Haase J, Muradyan P, Garrison J, and Wang K-N, "Airborne GPS radio occultation refractivity profiles observed in tropical storm environments," *Journal of Geophysical Research: Atmospheres*, vol. 120, no. 5, pp. 1690–1709, 2015.
- [21]. Sharawi MS, Akos DM, and Alois DN, "GPS C/N0 estimation in the presence of interference and limited quantization levels," *IEEE transactions on aerospace and electronic systems*, vol. 43, no. 1, pp. 227–238, 2007.
- [22]. Xu D and Morton Y, "A semi-open loop GNSS carrier tracking algorithm for monitoring strong equatorial scintillation," *IEEE Transactions on Aerospace and Electronic Systems*, vol. 54, no. 2, pp. 722–738, 2018.
- [23]. Niu F, Morton Y, Wang J, and Pelgrum W, "GPS carrier phase detrending methods and performances for ionosphere scintillation studies," in *25th International Technical Meeting of the Satellite Division of The Institute of Navigation, ION GNSS*, vol. 2000, 2012, pp. 1462–1467.
- [24]. Sokolovskiy S, Rocken C, Schreiner W, Hunt D, and Johnson J, "Postprocessing of L1 GPS radio occultation signals recorded in open-loop mode," *Radio science*, vol. 44, no. 02, pp. 1–13, 2009.
- [25]. Bar-Shalom Y, Li XR, and Kirubarajan T, *Estimation with applications to tracking and navigation: theory algorithms and software*. John Wiley & Sons, 2004.
- [26]. O'Driscoll C, Petovello MG, and Lachapelle G, "Choosing the coherent integration time for Kalman filter-based carrier-phase tracking of GNSS signals," *GPS solutions*, vol. 15, no. 4, pp. 345–356, 2011.

- [27]. “Datum exactime 6000 datasheet.” [Online]. Available: <https://accusrc.com/uploads/datasheets/datumexactime6000.pdf>
- [28]. Brown RG, Hwang PY et al., Introduction to random signals and applied Kalman filtering. Wiley New York, 1992, vol. 3.
- [29]. Tsui JB-Y, Fundamentals of Global Positioning System receivers: a software approach. John Wiley & Sons, 2005, vol. 173.
- [30]. Garrison JL, Walker M, Haase J, Lulich T, Xie F, Ventre BD, Boehme MH, Wilmhoff B, and Katzberg SJ, “Development and testing of the GISMOS instrument,” in 2007 IEEE International Geoscience and Remote Sensing Symposium IEEE, 2007, pp. 5105–5108.
- [31]. Gorbunov M, “Canonical transform method for processing radio occultation data in the lower troposphere,” Radio Science, vol. 37, no. 5, pp. 9–1, 2002.
- [32]. Collett I, Jade Morton Y, and Breitsch B, “Characterization and mitigation of interference between GNSS radio occultation and reflectometry signals for low altitude occultations,” in Proceedings of the 31st International Technical Meeting of the Satellite Division of The Institute of Navigation (ION GNSS+ 2018), vol. 2000, 2018, pp. 2848–2858.

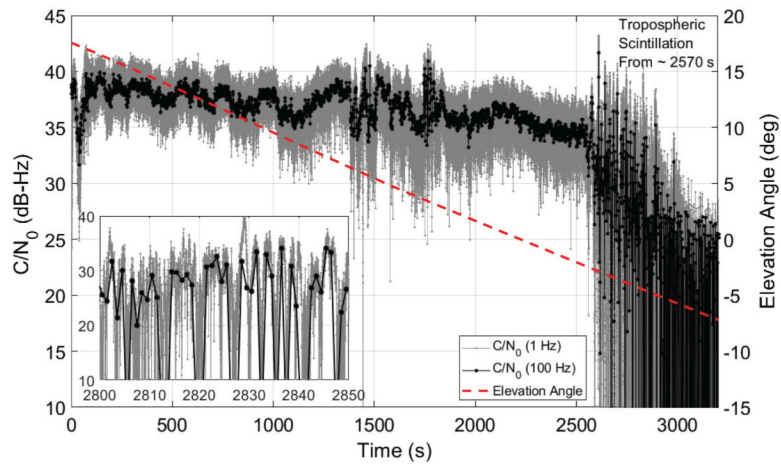


**Fig. 1.**  $C/N_0$  from OL tracking of setting PRN 12 GPS L1 signal, starting from UTC 10:00 AM on September 13<sup>th</sup>, 2010, recorded at 13 km altitude above the ocean near Puerto Rico

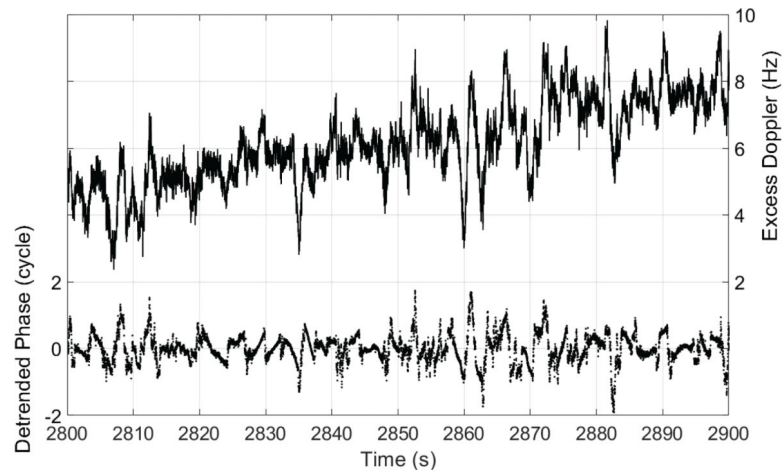


**Fig. 2.** Detrended carrier phase and excess Doppler frequency from OL tracking of setting PRN 12 GPS L1 signal, starting from 10:00 AM UTC on September 13<sup>th</sup>, 2010, recorded at 13km altitude above the ocean near Puerto Rico

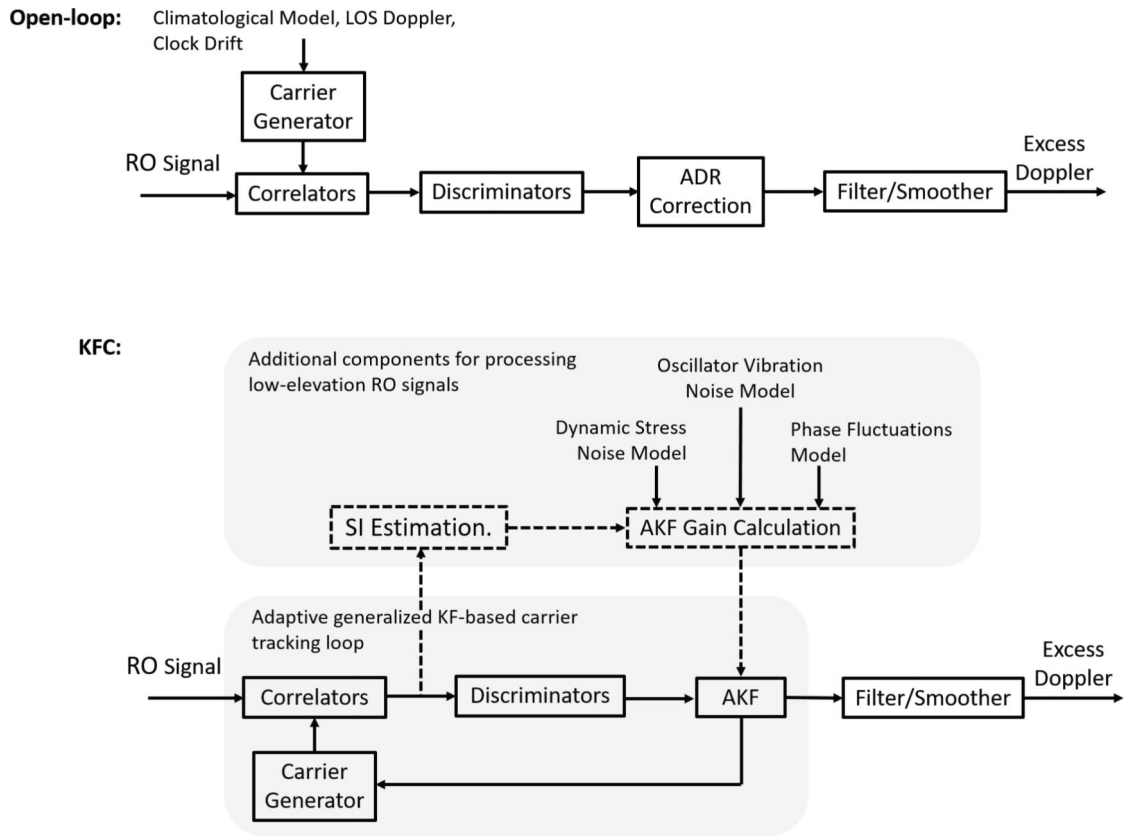


**Fig. 3.** Diagrams of Open-loop and Kalman filter-based CL carrier tracking of GNSS-RO signals

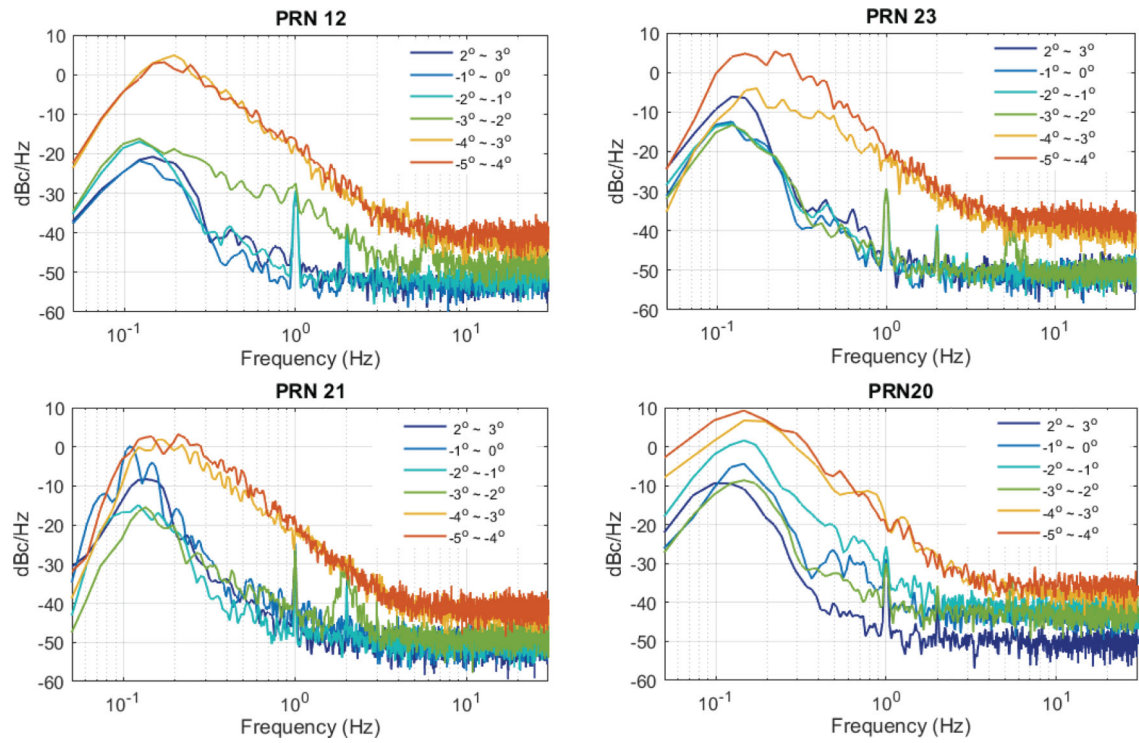


**Fig. 4.**

Power spectral densities of detrended phase fluctuations at various elevation angles (based on airborne GPS RO data collected on September 13<sup>th</sup>, 2010, at 13km altitude above the ocean near Puerto Rico).

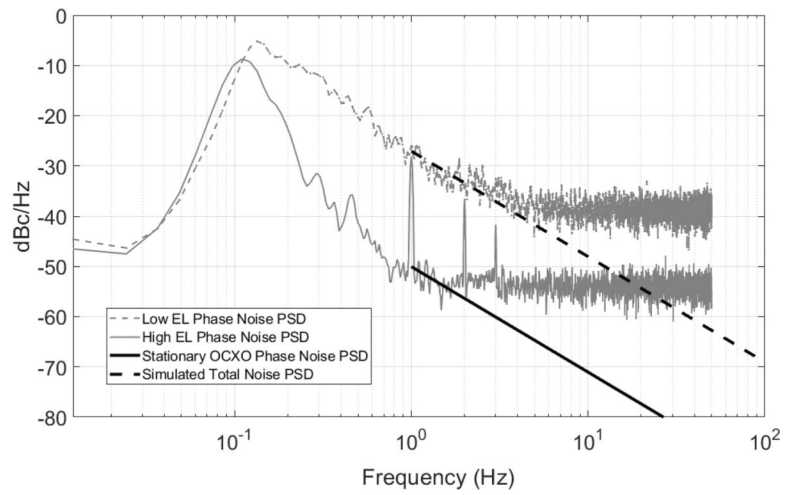


**Fig. 5.** Power spectral densities of carrier phase noise of high-elevation and low-elevation GPS PRN 12 signal on September 13<sup>th</sup>, 2010, stationary OCXO, and simulated total phase noise due to tropospheric scintillation and oscillator with vibration

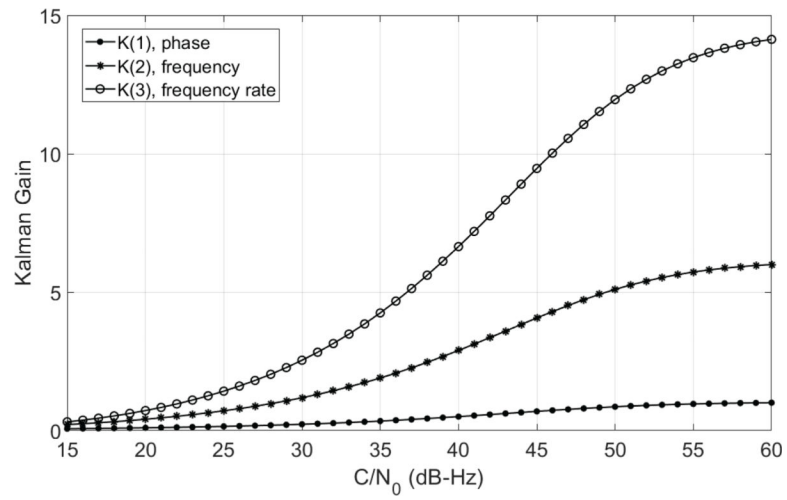


**Fig. 6.** Steady-state Kalman gain versus  $C/N_0$  for KFC tracking of low-elevation GPS RO signals affected by tropospheric scintillation

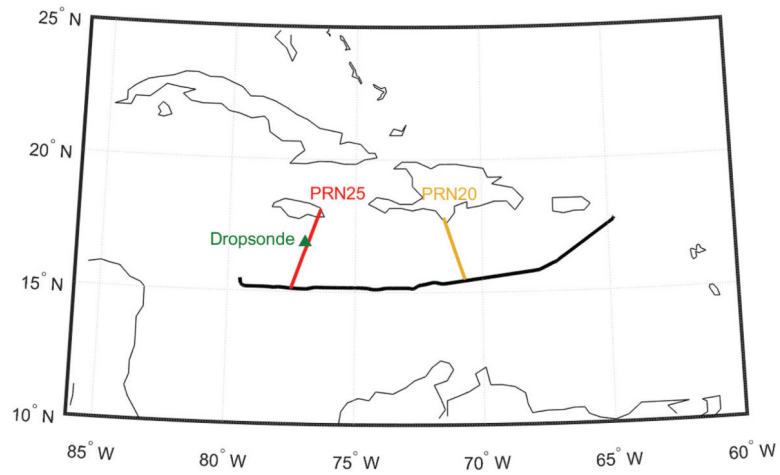
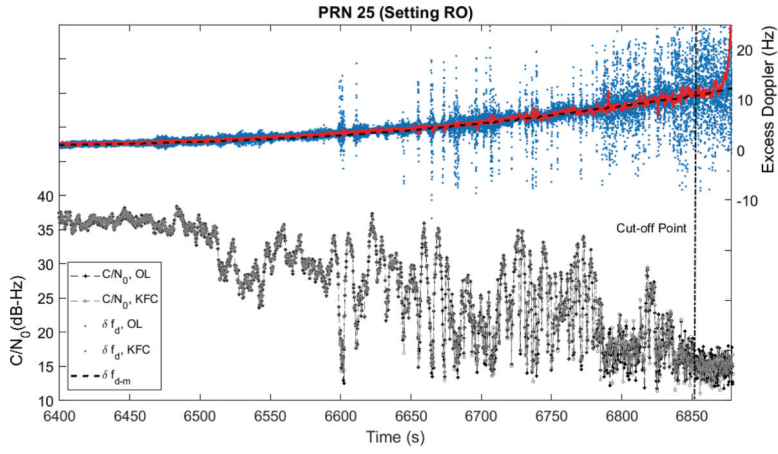
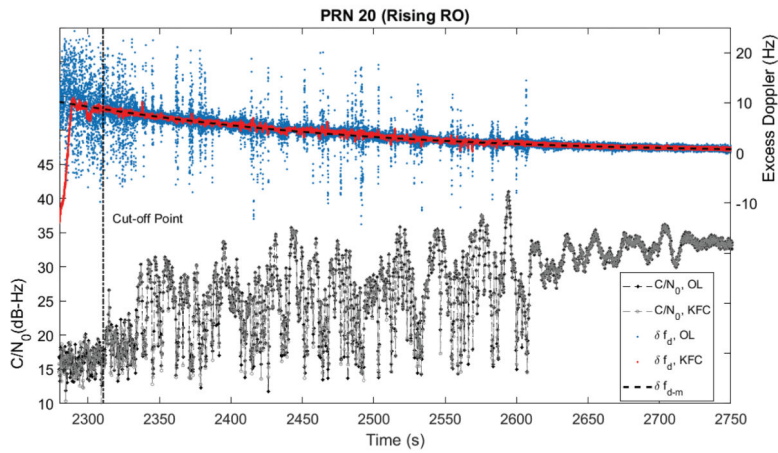


**Fig. 7.** The flight path during data collection on September 13<sup>th</sup>, 2010, above the ocean near Puerto Rico, the tangent point trajectories of PRN 25 and PRN 20 GPS RO events, and the location of a dropsonde experimnt



(a)



(b)

**Fig. 8.**  $C/N_0$  and excess Doppler ( $\delta f_d$ ) estimates from KFC and OL tracking, the climatological model for the excess Doppler used for OL tracking ( $\delta f_{d-m}$ ) for GPS L1 CA signal transmitted from PRN 25 (for elevation angle from  $-2.3^\circ$  to  $-5.4^\circ$ ) and PRN 20 (for elevation angle from  $-4.9^\circ$  to  $-1.8^\circ$ ) starting at 10:00 AM UTC on September 13<sup>th</sup>, 2010.

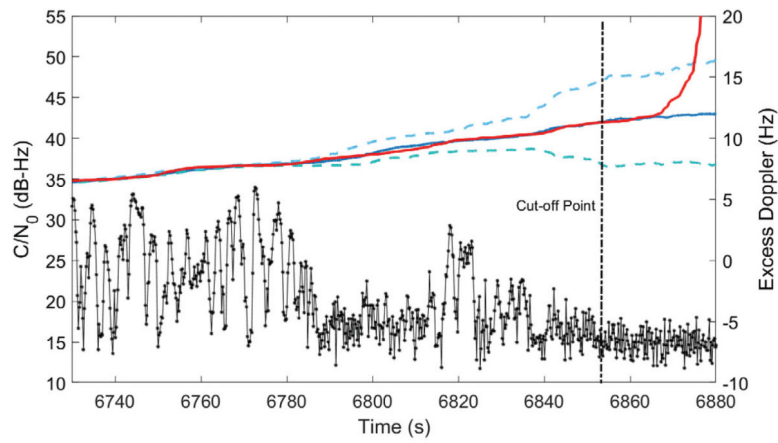


**Fig. 9.**  $C/N_0$  and filtered excess Doppler ( $\delta f_d$ ) estimates from KFC and OL tracking result of PRN 25 GPS L1 signal (with good climatological model and 5 Hz biased models) starting at 10:00 AM UTC on September 13<sup>th</sup>, 2010

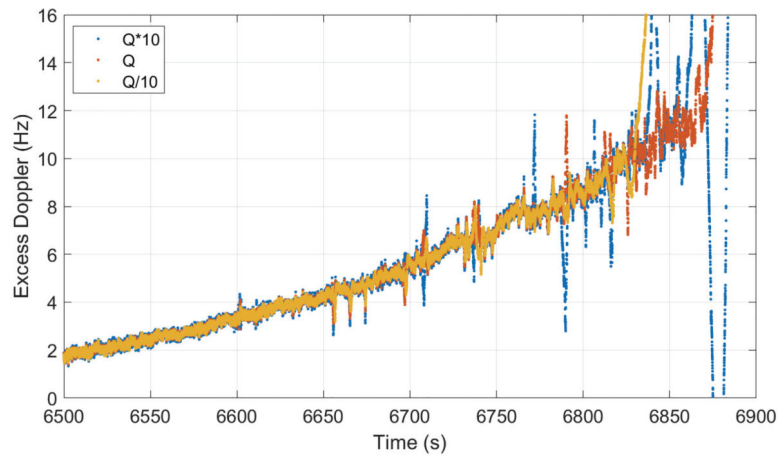


**Fig. 10.**  
Excess Doppler estimates from KFC Tracking using different process noise covariance matrices

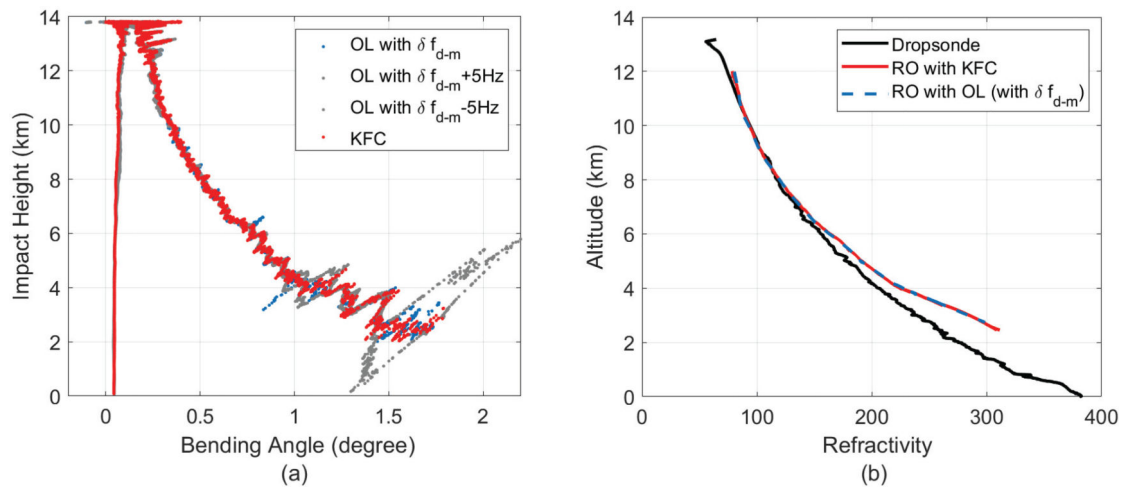


**Fig. 11.**

Retrieved bending angles and impact heights from KFC and OL (with good climatological model ( $\delta f_{d-m}$ ) and biased models) outputs of the setting RO event of PRN 25 GPS signal collected on September 13<sup>th</sup>, 2010, at 13.8km altitude above the ocean near Puerto Rico